RSC Advances

PAPER

View Article Online
View Journal | View Issue

Cite this: *RSC Adv.*, 2026, **16**, 26190

Mechanical grinding mediated lanthanum modified silicon carbide based nitride carbon composite material enhances adsorption of dye wastewater

Fanxia Zhang,†[ab] Yuan Min,†[b] Yuzhu Ji,[b] Jia Yang,*[b] Zhiliang Jin *[c] and Zhiqiang Wu *[ab]

Received 6th December 2025
Accepted 11th May 2026

DOI: 10.1039/d5ra09430e

rsc.li/rsc-advances

In this work, a novel La_x-g-C_3N_4@β-SiC composite adsorbent was synthesized by thermal polycondensation and mechanical methods. The samples were analyzed by characterization methods such as X-ray diffraction (XRD), scanning electron microscopy (SEM), and X-ray photoelectron spectroscopy (XPS). The La_{12}-g-C_3N_4@β-SiC sample presented a more porous layered morphology with a uniform pore structure. In addition, the application of these materials in the adsorption and removal of new organic pollutants was studied. The results show that La_{12}-g-C_3N_4@β-SiC has a good adsorption effect on both alizarin red S (ARS) and acid fuchsin (AF). Within 2.5 minutes, the adsorption efficiencies of ARS and AF were 93.23% and 70.33% respectively, and the corresponding adsorption capacities were 62.17 mg g^{-1} and 46.9 mg g^{-1} respectively. The kinetic and thermodynamic analyses of the adsorption process indicated that the adsorption of ARS and AF by La_{12}-g-C_3N_4@β-SiC conformed to the quasi-second-order kinetics and Langmuir adsorption isotherm model, with monolayer chemical adsorption being the main form. In addition, the composite material demonstrated excellent cycling stability and maintained outstanding adsorption performance even after eight repeated uses.

1. Introduction

At present, with the rapid development of industries including printing, dyeing, and coatings, the discharge volume of organic wastewater from these sectors is also increasing, posing substantial threats to the aquatic ecological environment and human health.[1–3] As typical acidic water pollutants, Alizarin red and acid fuchsin, feature complex compositions, high chromaticity, and adsorptive recalcitrance.[4,5] Traditional remediation techniques encounter substantial challenges in addressing these pollutants. Consequently, there is an urgent demand for the development of cost effective and highly efficient green materials for their treatment and remediation. The primary methods for treating acidic aqueous pollutants include physical methods, chemical methods, and biological methods.[6–8] Among these, physical adsorption methods have attracted extensive attention owing to their operational simplicity, availability of inexpensive raw materials, high processing efficiency, and eco-friendly properties.[9–11]

Notably, carbon nitride (g-C_3N_4), a novel inorganic non-metallic polymeric material developed over the past decade, has exhibited remarkable performance in the adsorption treatment of organic pollutants.[12–15] This efficacy can be attributed to its simple preparation process, abundant raw materials, and resistance to both acidic and alkaline conditions.[16,17] The distinctive electronic structure of g-C_3N_4, combined with its outstanding compatibility with other functional materials, contributes to its remarkable adsorption performance for organic pollutants.[18,19] However, the morphology of pure g-C_3N_4 bulk materials, typically prepared through calcination, often exhibits a layered structure, which presents limitations such as a small specific surface area, a sparse pore structure, and a narrow absorption response wavelength.[20–22] These factors substantially limit the adsorption performance of g-C_3N_4. Enhancing material properties through metal doping and modification has validated as an effective strategy. By doping g-C_3N_4 with metals, additional active sites are introduced, and improves electron transfer efficiency, thereby increasing the material's adsorption capacity. Furthermore, silicon carbide is a cost-effective and widely utilized inorganic semiconductor material, distinguished by its outstanding catalytic activity, particularly in applications such as adsorption, photocatalysis, and energy storage.[23,24] Silicon carbide possessed excellent mechanical strength, appropriate pore structure, and abundant

[a]*School of Civil and Hydraulic Engineering, Ningxia University, Yinchuan, 750021, P. R. China. E-mail: wuzqns@nxnu.edu.cn*

[b]*Ningxia Key Laboratory of Green Catalytic Materials and Technology, College of Chemistry and Chemical Engineering, Ningxia Normal University, Guyuan, 756099, P. R. China*

[c]*School of Chemistry and Chemical Engineering, Ningxia Key Laboratory of Solar Chemical Conversion Technology, North Minzu University, Yinchuan, 750021, P. R. China. E-mail: zl-jin@nun.edu.cn*

† Equal contribution.

surface hydroxyl functional groups, which effectively enhanced the dispersion and structural stability of the active components in the system, and could also generate a synergistic adsorption effect with the active components, thereby improving the overall adsorption performance.[25–27] Furthermore, β-SiC was also an efficient electron carrier and heterojunction material. By constructing a heterojunction interface with g-C_3N_4, not only could the recombination of photogenerated electron–hole pairs in g-C_3N_4 be effectively suppressed, but also the specific surface area and structural stability of the composite material could be significantly improved.[28] Due to its stable structure, excellent surface chemical properties, and pore structure, silicon carbide became a key component for achieving efficient and stable adsorption. Research has demonstrated that the catalytic performance of silicon carbide can be markedly improved when it is combined with carbon nitride.[29,30] This improvement is attributed to the complementary band gaps of carbon nitride and silicon carbide, which facilitate the formation of a type II heterojunction through chemical interactions.[31] This structural configuration facilitates the separation and transfer of photogenerated electron–hole pairs, thereby improving the performance of the material. In 2017, Huang *et al.* first synthesized g-C_3N_4/SiC material by attaching silicon carbide to the surface of carbon nitride and studied its photocatalytic hydrogen production performance.[32] The results indicated that the BET surface area of the g-C_3N_4/SiC material was 15.0 m^2 g^{-1}, with a hydrogen production rate of 182 μmol g^{-1} h^{-1}, which is 3.4 times greater than that of pure g-C_3N_4. Subsequently, Gan *et al.* designed SiC nanoparticles and g-C_3N_4 nanosheets by constructing type II heterostructures and applied them to the adsorption of methyl orange (MO) wastewater.[31] The findings revealed that the adsorption rate of MO by this material reached 55% within one hour. Additionally, the *Z*-shaped heterostructure SiC/g-C_3N_4 composite material prepared by Guo *et al.*[33] exhibited a adsorption rate of 71.1% for tetracycline within three hours under visible light conditions. Similarly, there have been numerous studies on various typical organic pollutants, including methyl orange and ciprofloxacin, in other silicon carbide and nitride carbon composite materials, including Cu_2O-SiC/g-C_3N_4,[34] SiC/g-C_3N_4,[35] 3D-SiC/C_3N_4,[36] Ni/SiC/CNNS,[37] SiCf/g-C_3N_4.[33] Nevertheless, this research is typically coupled with photocatalytic processes, which substantially elevate both energy consumption and operational complexity. Additionally, the SiC adopted in many existing studies is generally commercial-grade micro-nano powder, whose crystalline phase is typically consists of a mixture of α-SiC and β-SiC.[38] These works may lack design and performance comparison experiments involving pure nanocrystalline SiC and g-C_3N_4 composite materials. Additionally, limitations such as the relatively small specific surface area of the prepared materials impede the improvement of their functional performance.

In addition, the cage-structured interactions of rare earth metals facilitate the enrichment of organic pollutants on the catalyst surface, highlighting their significant potential in the fabrication of composite materials with high adsorption efficiency. Lanthanide metal ions serve as exceptional materials for the adsorption and adsorption of organic pollutants. This performance arises from the ability of lanthanide metal ions, when used as dopants, to reduce the particle size of the host material to a certain extent, thereby enhancing the specific surface area and catalytic activity of the material.[39] Yin *et al.* immobilized $La(OH)_3$ nanoparticles on C_3N_4, effectively limiting the aggregation of the material and enhancing its phosphate adsorption capacity, which reached a maximum of 148.35 mg g^{-1}.[40] Prasanna *et al.* doped erbium metal into graphite carbonitride, significantly improving the adsorption and adsorption of tetracycline (TC).[41] Additionally, Yu *et al.* synthesized cerium metal-modified g-C_3N_4 nanosheets using a thermal shrinkage method, achieving over 80% adsorption efficiency for various dyes within 2.5 hours.[42] From the perspective of energy consumption, adsorption generally proceeds under dark reaction conditions, without the requirement for additional energy input. This feature differs significantly from photocatalytic processes, which depend on light energy as a driving force. In the previous research of our team, we have been dedicated to developing a series of highly efficient catalytic and adsorptive materials. We successively prepared protonated g-C_3N_4/β-SiC composite materials.[43] This material demonstrated excellent performance in the photocatalytic adsorption of alizarin red wastewater, with an adsorption efficiency as high as 99.9% and good cycling stability. Furthermore, lanthanum-modified mesoporous g-C_3N_4 was synthesized, significantly enhancing its adsorption and adsorption performance for tetracycline and acid fuchsin.[44] Furthermore, we enhanced the photocatalytic performance of g-C_3N_4/β-SiC through acid protonation treatment.[45] It was found that protonation treatment not only increased the specific surface area of the material but also significantly reduced the recombination probability of photogenerated electron–hole pairs. Among the numerous methods for preparing and modifying functional nanomaterials, the mechanochemical method has gained significant attention in recent years due to its simplicity of operation, solvent-free nature, and environmental friendliness, especially in the fields of environmental remediation and the synthesis of adsorption materials. For instance, Fathy *et al.* used a planetary ball mill to conduct mechanical chemical activation on discarded cathode ray tubes, successfully extracting approximately 85% of lead using ethylenediaminetetraacetic acid (EDTA), demonstrating the high efficiency of this method in waste resource utilization.[46] This method promoted the solid-phase chemical reactions induced by mechanical force by disrupting the molecular structure within the material, thereby increasing the number of active sites and expanding its application scope in the environment.

On the basis of the aforementioned research progress, this work aimed to combine rare earth metal-doped g-C_3N_4 with structurally stable β-SiC supports to construct La_x-g-C_3N_4@β-SiC composite materials, and systematically investigate their adsorption performance and mechanism for dye wastewater such as alizarin red and acid fuchsin. This work was expected to provide new strategies for the development of efficient water treatment materials. Lanthanum-modified carbon nitride supported silicon carbide mesoporous composites (La_x-g-C_3N_4@β-SiC) were synthesized using melamine treated with dilute

sulfuric acid, lanthanum nitrate hexahydrate and nanoscale β-SiC as raw materials by combining mechanochemical and thermal polymerization methods. The structural characteristics and pore size distribution of La_x-g-C_3N_4@β-SiC were analyzed using techniques such as SEM, XPS, and BET. Furthermore, the adsorption performance of the material toward alizarin red and acid fuchsin was systematically investigated *via* screening and optimization. Meanwhile, the adsorption mechanism of the optimized material La_{12}-g-C_3N_4@β-SiC toward organic pollutants was analyzed using adsorption isotherms, kinetics models, and thermodynamic fitting equations.

2. Experimental section

2.1 Synthesis of g-C_3N_4

Slowly dissolve 10 g of melamine in a mixture of 35 mL of ethylene glycol and 100 mL of dilute sulfuric acid (0.1 mol L^{-1}), and stir for 50 minutes to form a homogeneous solution. After 24 hours of sedimentation, the white precipitate was collected by suction filtration and washed 3 to 4 times with ethanol and deionized water. After being dried overnight in an oven at 60 °C and ground into powder, A white powder protonated precursor can be obtained, labeled as sample A. The above steps are repeated multiple times, and A total of 70–80 g of sample A is collected. Weigh 10 g of the precursor and calcine it in an air atmosphere (calcination conditions: increase the temperature from room temperature to 350 °C at a rate of 2 °C min^{-1} and hold for 1 hour; continue to increase the temperature at a rate of 5 °C min^{-1} and hold for 550 °C for 3 hours). After cooling to room temperature, the protonated graphite phase carbon nitride material was obtained and labeled as g-C_3N_4.

2.2 Synthesis of g-C_3N_4@β-SiC

Melamine (5 g) treated with dilute sulfuric acid and β-SiC powder (0.2 g) were simultaneously added to the ball mill jar. They were ball-milled at 600 rpm for 30 minutes in a planetary ball mill, and the powder was removed from the ball mill jar. The powder of the above-mentioned mixture was taken out and transferred to an alumina crucible. It was calcined in an air atmosphere (calcination conditions: heated from room temperature to 350 °C at a rate of 2 °C min^{-1} and held for 1 h; then heated to 550 °C at a rate of 5 °C min^{-1} and held for 3 h). After cooling to room temperature, the g-C_3N_4@β-SiC sample was obtained.

2.3 Synthesis of La_x-g-C_3N_4@β-SiC

Lanthanum nitrate hexahydrate ($La(NO_3)\cdot 6H_2O$) of different masses and melamine treated with 5 g of dilute sulfuric acid were simultaneously added to the ball mill jar, and β-SiC powder (0.2 g) was added. The dosage of lanthanum nitrate hexahydrate should mainly be 2% to 16% of melamine treated with 5 g dilute sulfuric acid. The powder was ground at 600 rpm for 30 minutes in a planetary ball mill and then removed from the ball mill jar. The powder of the above-mentioned mixture was taken out and transferred to an alumina crucible. It was calcined in an air atmosphere (calcination conditions: heated from room temperature to 350 °C at a rate of 2 °C min^{-1} and held for 1 hour; then heated to 550 °C at a rate of 5 °C min^{-1} and held for 3 hours). After cooling to room temperature, the preparation of lanthanum metal-doped protonated carbon nitride @β-SiC material was obtained. The prepared samples were recorded as: La_2-g-C_3N_4@β-SiC; La_4-g-C_3N_4@β-SiC; La_6-g-C_3N_4@β-SiC; La_8-g-C_3N_4@β-SiC; La_{10}-g-C_3N_4@β-SiC; La_{12}-g-C_3N_4@β-SiC; La_{14}-g-C_3N_4@β-SiC; La_{16}-g-C_3N_4@β-SiC.

2.4 Characterization

X-ray diffraction (XRD) patterns were obtained on a Bruker D8 Advance diffractometer (Germany) with a copper target. Fourier Transform Infrared (FT-IR) spectra were recorded in the range of 400–4000 cm^{-1} on a Thermo Nicolet IS5 spectrometer. The specific surface area and porosity were analyzed by the Brunauer–Emmett–Teller (BET) method using a Micromeritics ASAP 2420 fully automated analyzer. Morphological analysis was conducted *via* scanning electron microscopy (SEM) on a ZEISS Sigma 360 instrument (Germany) and by transmission electron microscopy (TEM) along with high-resolution TEM (HRTEM) on an FEI Talos F200x microscope (USA). Surface chemical states were examined by X-ray photoelectron spectroscopy (XPS) on a Thermo Fisher Nexsa system. Photocatalytic performance was evaluated at room temperature by monitoring absorbance changes with a TU-1901 double-beam UV-Vis spectrophotometer (Perse, China). Finally, liquid chromatography-mass spectrometry (LC-MS) data in positive ion mode were collected using a Waters G2-S QTOF instrument.

2.5 Adsorption performance evaluation experiments

Taking tetracycline as the adsorption object as an example, the adsorption properties of g-C_3N_4, g-C_3N_4@β-SiC, and La_x-g-C_3N_4@β-SiC samples. During the adsorption performance test, the experimental device used was a photochemical reactor, and the light source switch of the testing equipment was always kept off throughout the process to ensure that the entire adsorption process was carried out in a dark environment. Evenly disperse 40 mg of the sample in a 50 mL, 20 mg L^{-1} wastewater solution. Dark react and stir for 30 minutes in a photochemical reaction instrument. During the adsorption process, samples were taken every ten minutes. The absorbance was measured using a UV-visible spectrophotometer at a wavelength of 359 nm. Before the test, the samples were first filtered through a microporous membrane (with a specification of 0.22 μm), and then placed in a 1 cm × 1 cm cuvette. After completing one experimental cycle according to the above steps, the adsorbent samples were subjected to centrifugation for recovery. Then, they were washed three times with deionized water and ethanol, and subsequently dried at 60 °C for use in the next cycle.

3. Results and discussion

3.1 Microscopic morphology and internal structure

The synthetic pathway of the La_x-g-C_3N_4@β-SiC adsorbent is shown in Fig. 1. The crystallinity and structural properties of g-C_3N_4, g-C_3N_4@β-SiC, and La_x-g-C_3N_4@β-SiC adsorbents were

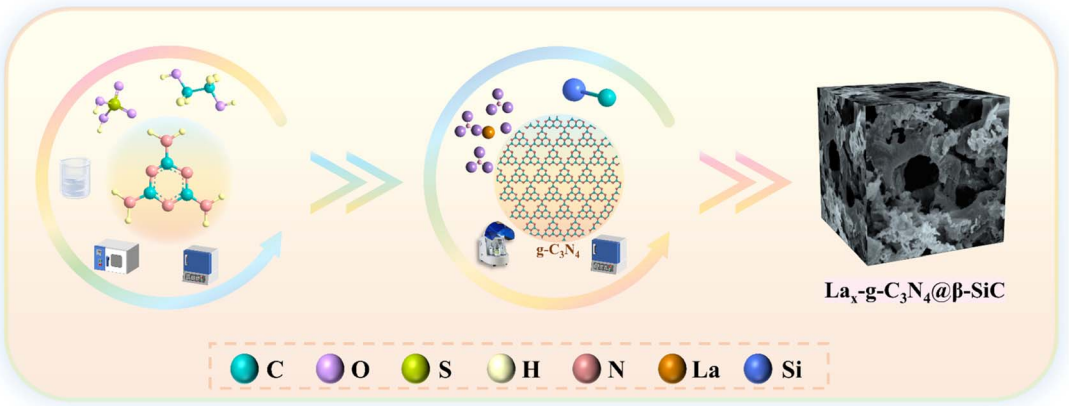

Fig. 1 The schematic diagram of the preparation process of the sorbent samples.

analyzed by X-ray powder diffraction (XRD) and Fourier transform infrared spectroscopy (FT-IR). As shown in Fig. 2a, the samples after introducing β-SiC and the rare earth metal lanthanum retain the intrinsic characteristics of the original g-C_3N_4 adsorbent. 13.1° and 27.3° in the XRD pattern correspond to the (100) and (002) crystal planes of g-C_3N_4 respectively.[45–48] With the addition of β-SiC and the rare earth metal lanthanum, the peak signals of the (100) and (002) crystal planes gradually decrease. The 35.8°, 41.5°, 60.2°, 72.0°, and 75.5° XRD of g-C_3N_4@β-SiC correspond respectively to the (111), (200), (220), (311), and (222) crystal planes in β-SiC.[45,49–51] With the continuous increase of the doping amount of lanthanum element in rare earth metal, the peaks of each crystal plane of g-C_3N_4@β-SiC gradually decrease. The changes in the signal intensity of the above crystal plane peaks confirmed the successful preparation of g-C_3N_4@β-SiC and La$_x$-g-C_3N_4@β-SiC.

To further explore its internal structural characteristics, Fourier Transform infrared spectroscopy (FT-IR) analysis was carried out (Fig. 2b). The FT-IR spectra confirm the characteristic structure of the g-C_3N_4 adsorbent. A broad absorption peak near 3085.2 cm^{-1} corresponds to the N–H stretching vibration.[45–48] The region between 1227.0 and 1625.8 cm^{-1} is associated with the stretching vibrations of C–N and C=N bonds within the aromatic ring system.[52,53] Notably, the distinct peak at 804.2 cm^{-1} is attributed to the vibrational mode of the triazine ring, a defining feature of g-C_3N_4.[45,52] With the increase of doping amounts of SiC and rare earth metal La, the peak intensity gradually decreases. The FT-IR spectrum of the La$_x$-g-C_3N_4@β-SiC adsorbent exhibits a distinct feature not present in

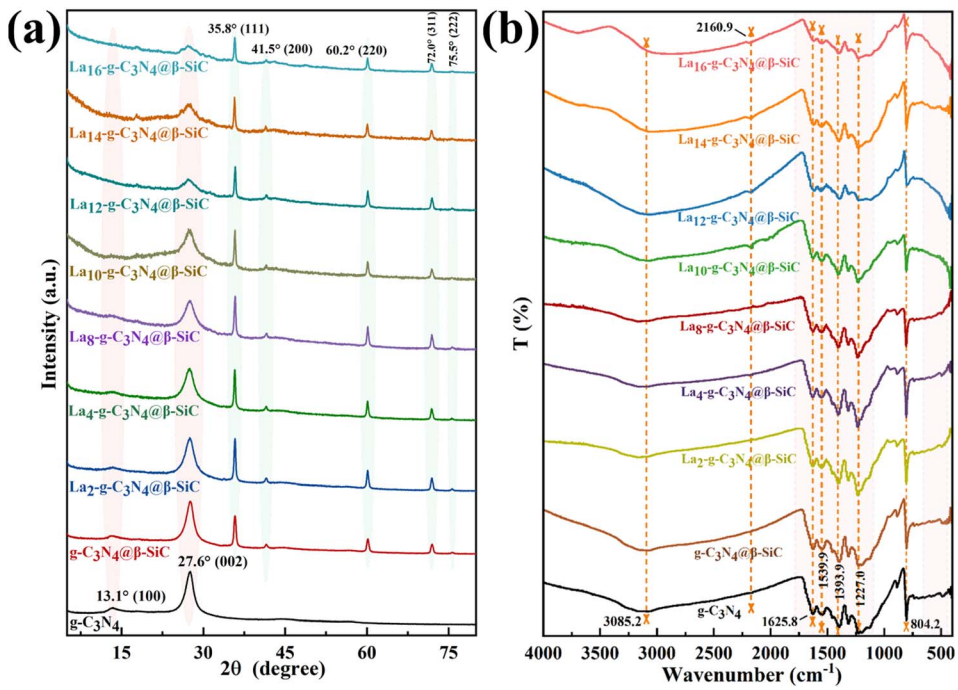

Fig. 2 (a) XRD of g-C_3N_4, g-C_3N_4@β-SiC, and La$_x$-g-C_3N_4@β-SiC; (b) FT-IR spectra of g-C_3N_4, g-C3N4@β-SiC, and La$_x$-g-C_3N_4@β-SiC.

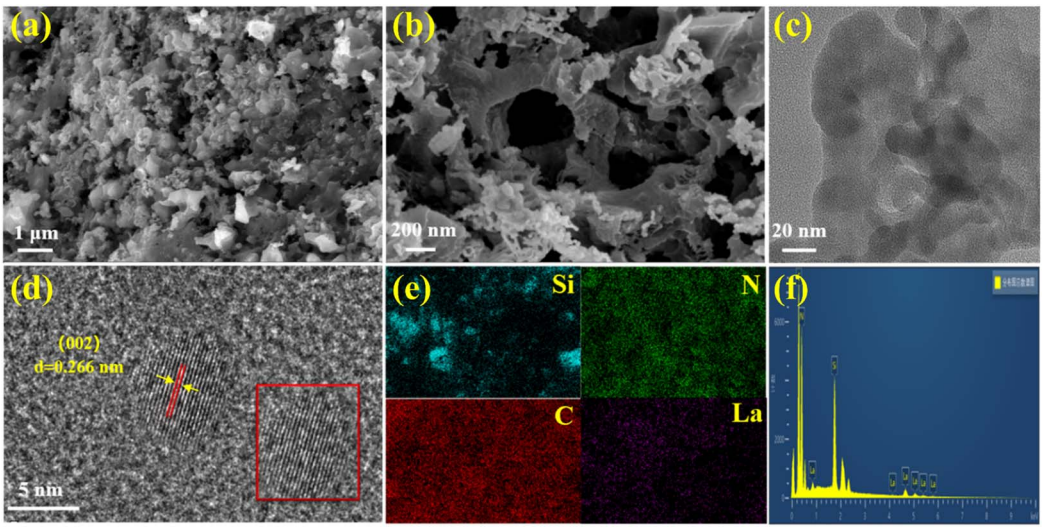

Fig. 3 (a and b) SEM micrographs of La_{12}-g-C_3N_4@β-SiC; (c) the TEM analysis of La_{12}-g-C_3N_4@β-SiC; (d) the HRTEM analysis of La_x-g-C_3N_4@β-SiC; (e and f) EDS elemental mapping demonstrating homogeneous spatial distribution of Si, N, C, and La in La_x-g-C_3N_4@β-SiC.

pure g-C_3N_4: a characteristic peak emerges at 2160.9 cm^{-1} under higher La doping levels. The intensity of this peak increases progressively with greater La content.[44,53] This signal is attributed to the stretching vibration of a C≡N bond, rather than aromatic C–N. This spectral change suggests that La doping partially disrupts the triazine ring structure of g-C_3N_4.

The microstructure and morphology were analyzed through SEM and HRTEM characterization, and the results are shown in Fig. 3a–f. Fig. 3a shows the SEM image of La_{12}-g-C_3N_4@β-SiC, presenting a distinct snowflake-like flocculent packing structure and the appearance of some small pore structures. From Fig. 3b, it can be seen that the morphology has a certain layered stacking structure and a skeleton structure similar to that, showing a more porous layered structure with different pores of different diameters, which may lead to an increased specific surface area of the material. It also indicates that the introduction of lanthanum and β-SiC has played a certain promoting role in the morphology modification of carbon nitride polymer materials. In addition, the EDS spectra and Mapping diagrams show that related elements such as Si, N, C, and La are all present in the samples, further indicating the successful preparation of La_{12}-g-C_3N_4@β-SiC. Furthermore, through the plasma spectrometer (ICP-OES) test, it was found that the content of lanthanum in the La_{12}-g-C_3N_4@β-SiC composite adsorbent was 11.6%, which corresponded to the doping amount of lanthanum in this composite material.

The BET characterization analysis of g-C_3N_4, g-C_3N_4@β-SiC, and La_x-g-C_3N_4@β-SiC revealed type IV N_2 adsorption–desorption isotherms of these adsorbent materials with H3 hysteresis loops (Fig. 4a). This is the characteristic of stratified porous materials containing mesopores (2–50 nm) and macropores (>50 nm), and the main pore size distribution range (0–25 nm range) confirms the mesoporous materials (Fig. 4b). With the introduction of β-SiC and La elements, the adsorbent shows a trend of either increasing or decreasing in terms of specific surface area. This phenomenon may occur because β-SiC fills some of the pores of g-C_3N_4 or forms a dense interface with g-C_3N_4, reducing the specific surface area. The composite

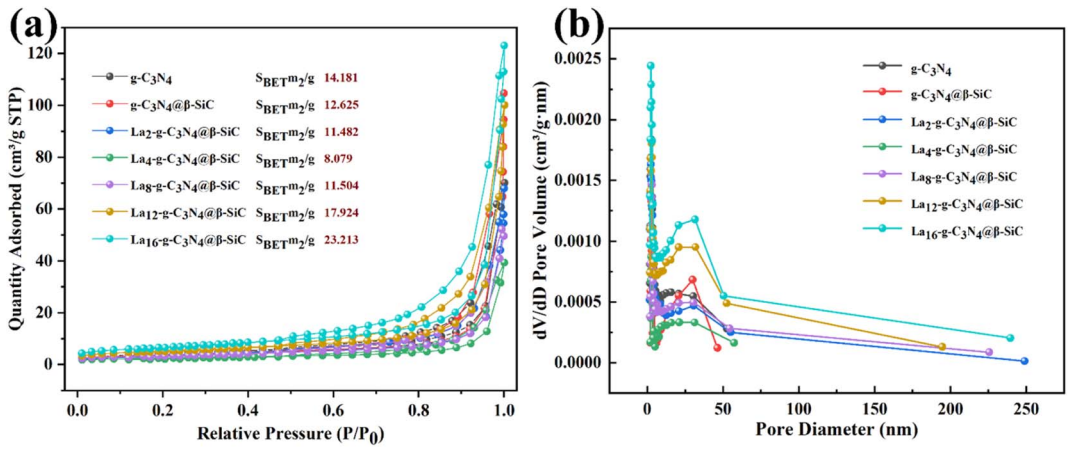

Fig. 4 (a) The nitrogen adsorption–desorption isotherms of g-C_3N_4, g-C_3N_4@β-SiC, and La_x-g-C_3N_4@β-SiC; (b) the aperture distribution diagrams of g-C_3N_4, g-C_3N_4@β-SiC, and La_x-g-C_3N_4@β-SiC.

adsorbent with a low doping amount of La element is slightly lower than the original g-C_3N_4, which might be caused by clogged pores. Under a higher doping amount, the specific surface area is significantly higher than that of the original g-C_3N_4, indicating that the content of high La element further increases the porosity and the pore volume further increases, suggesting that the porosity is enhanced under a higher doping amount, providing sufficient space for pollutant adsorption. In addition, the BET test results showed that the specific surface area was positively correlated with the adsorption performance. When the doping amount of lanthanum nitrate hexahydrate increased from 2% to 12%, the corresponding specific surface area rose from 11.48 $m^2\ g^{-1}$ to 17.92 $m^2\ g^{-1}$, and the adsorption capacity of tetracycline pollutants significantly increased from 6.55 mg g^{-1} to 35.05 mg g^{-1}. This indicated that when the doping amount of lanthanum increased, the specific surface area showed a synchronous growth trend, and the increase in specific surface area was a key factor in improving adsorption performance. Meanwhile, a positive correlation between pore volume and adsorption performance was also observed as the doping amount increased from 2% to 12%, the corresponding pore volume increased from 0.09 $cm^3\ g^{-1}$ to 0.14 $cm^3\ g^{-1}$, indicating that the increase in pore volume was also an important influencing factor for improving adsorption performance. The nitrogen adsorption–desorption and pore size analysis indicated that the loading amount of lanthanum was the key factor regulating the pore structure of g-C_3N_4@β-SiC, providing a theoretical basis for subsequent adsorption applications.

In order to deeply analyze the chemical composition and electronic valence state of the La_{12}-g-C_3N_4@β-SiC composite adsorbent, the characteristic peaks of the X-ray photoelectron spectra of C, N, O, and La in La_x-g-C_3N_4@β-SiC were analyzed in this work. Full-spectrum analysis indicated (Fig. 5a) that La_{12}-g-C_3N_4@β-SiC was composed of C, N, O, La, and Si elements. As the content of Si element was lower than the detection limit of the test, the distinct peak signal of the fine spectrum of XPS could not be detected. However, the XPS full spectrum and EDS mapping can also confirm that La_{12}-g-C_3N_4@β-SiC contains Si elements. These intrinsic structural features jointly support the application potential of La_{12}-g-C_3N_4@β-SiC as an efficient adsorbent. In the C 1s fine spectrum (Fig. 5b), the signal peak at the binding energy of 284.80 eV corresponds to the C–C bond (sp^2 or sp^3 hybrid carbon), which are respectively the C–Si covalent skeletons of β-SiC (in β-SiC, carbon and silicon are covalently bonded).[43,45] There are a few C–C defects at the edges and the edge areas of g-C_3N_4 (carbon sites that are not fully conjugated at the edges of graphite-like structures). The peak signal at 286.39 eV belongs to the N–$(C)_3$ bond and is a characteristic peak of g-C_3N_4. g-C_3N_4 takes the tri-*s*-triazine ring as the basic unit. Each carbon atom coordinates with three nitrogen atoms to form a conjugated skeleton. The existence of this peak proves that the main structure of g-C_3N_4 has not been damaged. The signal peak at 289.26 eV corresponds to the C═N–C bond.[44] During the preparation or storage of adsorbents, the surface carbon sites react with oxygen in the air to form polar carbonyl groups. These polar sites can adsorb polar pollutants such as ARS (alizarin red S) and AF (acid fuchsin) through hydrogen bonds and dipole interactions, thereby enhancing the adsorption performance. Fig. 5c shows the fine spectrum of N 1s. The signal peak with a binding energy of 399.62 eV belongs to the low-valent nitrogen or the nitrogen interacting with La. Among them, La^{3+} (the main valence state of lanthanum) is a cation and can form coordination interaction (La–N bond) with the nitrogen atom with strong electronegativity in g-C_3N_4, changing the electron cloud density of nitrogen. This electronic interaction will adjust the surface charge distribution of the adsorbent, which is conducive to the adsorption of anionic pollutants

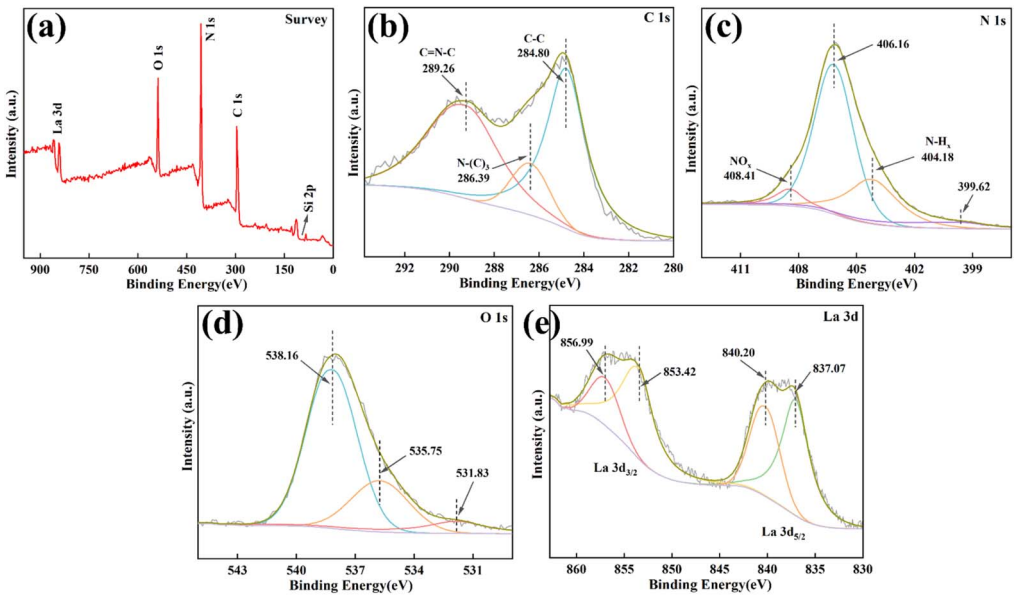

Fig. 5 The XPS full spectrum (a), C 1s spectrum (b), N 1s spectrum (c), O 1s spectrum (d), and La 3d spectrum (e) of La_{12}-g-C_3N_4@β-SiC adsorbent.

(such as ARS and AF dissociating into anions in water). The signal peaks of 408.41 eV and 404.18 eV correspond respectively to the NO group (nitrogen oxides) and the N–H bond (amino group), which help the adsorbent to fully contact the pollutants in the aqueous solution.[43,45] It can enhance the adsorption capacity by reacting with the sulfonic acid groups (–SO_3H) and hydroxyl groups (–OH) of the pollutants through hydrogen bonds. The signal peak at 406.16 eV corresponds to the N–$(C)_3$ bond and is a characteristic peak of g-C_3N_4, demonstrating that the conjugated carbon nitride skeleton of g-C_3N_4 remains intact after recombination (introducing β-SiC) and doping (introducing La). The O 1s fine spectrum shows three types of oxygen-containing species (Fig. 5d), and the signal peak at 538.16 eV corresponds to adsorbed water or hydroxyl groups (–OH), promoting the mass transfer process in the aqueous phase. The 535.75 eV signal peak corresponds to C=O bonds (carbonyl groups) or N=O bonds (nitro groups).[44] These polar oxygen-containing groups can enhance the interaction between adsorbents and polar pollutants and are important "active sites" in the adsorption process. The signal peak at 531.83 eV belongs to the Si–O bond.[45,47] The presence of the Si–O bond not only enhances the hydrophilicity of β-SiC but also forms hydrogen bonds with pollutants through Si–O–H (silanol groups), further strengthening the adsorption capacity. The 3d spectrum of La (Fig. 5e) reveals the valence state and interaction of lanthanum, presenting typical spin–orbit splitting characteristics. Multiple sets of characteristic peaks appeared in the spectrum, and their peak positions were consistent with those of the characteristic peaks of La^{3+} (the stable valence state of lanthanum) in the reported literature, proving that La exists in the material in the form of La^{3+}. As a cationic site, La can adsorb anionic pollutants such as ARS and AF through electrostatic interaction. It can also interact with g-C_3N_4 and β-SiC through La–N and La–O bonds to regulate the electronic structure and distribution of surface-active sites of the material, thereby indirectly enhancing the adsorption performance.

3.2 Investigation of adsorption performance

Taking tetracycline as the adsorption performance test object, the performance of a total of 10 groups of samples, including g-C_3N_4, g-C_3N_4@β-SiC, and La_x-g-C_3N_4@β-SiC, was investigated. As can be seen from Fig. 6a, with the continuous increase of La doping amount, the adsorption performance gradually improves, especially when the doping amounts are 12%, 14% and 16%, the adsorption effect is more obvious. Considering the economy of the material, La_{12}-g-C_3N_4@β-SiC adsorbent with a doping amount of 12% was adopted as the object for the subsequent adsorption performance investigation. Furthermore, the adsorption performance of the adsorbent for different emerging organic pollutants was investigated (Fig. 6b), and the performance of the La_{12}-g-C_3N_4@β-SiC adsorbent was evaluated to determine whether it has wide applicability. Under the same conditions, 40 mg of La_{12}-g-C_3N_4@β-SiC adsorbent was dispersed to remove 50 mL of 20 mg L^{-1} of different wastewater. The appearance changes before and after were recorded (Fig. 6c) and the adsorption efficiency. As can be seen from the figure, alizarin red S (ARS) has the best adsorption efficiency, followed by acid fuchsin (AF). Alizarin red S solution was mainly used for subsequent condition screening. Subsequently, the adsorption effects of La_{12}-g-C_3N_4@β-SiC adsorbent on alizarin red (ARS) wastewater with different feed amounts of 50 mL and 20 mg L^{-1} were investigated by dispersing La_{12}-g-C_3N_4@β-SiC adsorbent at feed amounts of 5 mg, 10 mg, 15 mg, 20 mg, 25 mg, 40 mg, and 60 mg (Fig. 6d). The adsorption rates of 20 mg, 40 mg, and 60 mg were all above 95%. To save the amount of adsorbent used, 20 mg was adopted as the subsequent feeding amount for condition screening. Then, the adsorption efficiency of organic pollutants at different reaction times was investigated with sampling time intervals of 30 seconds, 60 seconds, and 90 seconds (Fig. 6e). The results showed that within a 30-second time interval, the adsorption effect did not change significantly, so short-time sampling had little impact on the change in adsorption effect. The adsorption effect under different pH values was further investigated

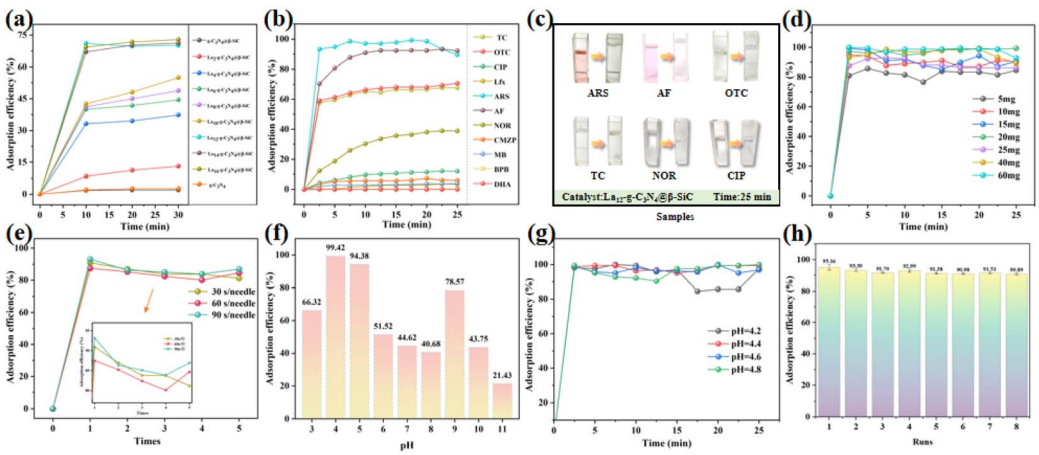

Fig. 6 (a) Screen different proportions; (b) screen different pollutants; (c) appearance changes before and after adsorption of different pollutants; (d) screen different feed quantities; (e) screen different sampling times; (f) investigation of adsorption performance at different pH values; (g) detailed investigation of adsorption performance at pH values ranging from 4.2 to 4.8; (h) evaluation of catalyst reusability.

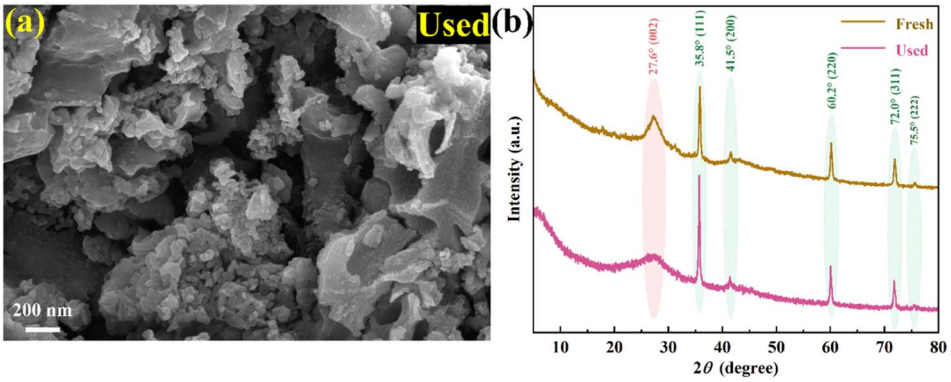

Fig. 7 The SEM (a) and XRD (b) graphs of La_{12}-g-C_3N_4@β-SiC adsorbent before and after recycling.

(Fig. 6f), and the optimal pH value was screened out as 4. Subsequently, the pH value was refined to 4.2–4.8 to investigate its adsorption effect (Fig. 6g), in order to determine the optimal reaction condition as the pH value of 4. To investigate the recovery performance of the adsorbent under these optimal conditions (Fig. 6h), three independent replicate experiments were conducted. The results demonstrated that after 8 consecutive cycles, the adsorbent maintained an average adsorption efficiency of 90%, indicating excellent cyclic stability.

The XRD and SEM analyses after the cycle confirmed that there were no significant changes in the morphology, structure and internal properties of the material. The surface morphology remained consistent with that before cycling, indicating that its structure demonstrated excellent adsorption and cycling stability during the reaction process (Fig. 7a and b). This result not only verifies the rationality of the composite material design, but also provides a key experimental basis for the subsequent construction of an efficient and stable adsorption system. In addition, we compared the catalyst used in this work with the catalysts that have been reported (Table 1). The adsorption rate of La_{12}-g-C_3N_4@β-SiC could reach 93% within 30 minutes when it was used to adsorb ARS. The adsorption capacity was higher than that of other catalysts. Moreover, the adsorption rate remained stable at 90% after 8 consecutive cycles, and the preparation cost of the adsorbent was relatively low.

3.3 Adsorption mechanical fitting and analysis

The kinetics study was conducted by mixing La_{12}-g-C_3N_4@β-SiC (20 mg) with ARS (50 mL, 20 mg L^{-1}) solution and AF (50 mL, 20 mg L^{-1}) solution. The adsorption kinetics was studied by using the quasi-first-order and quasi-second-order models. The linear forms of the two models are respectively expressed as formulas (1) and (2):

$$\log(q_e - q_t) = \log q_e - \frac{k_1 t}{2.303} \quad (1)$$

$$\frac{t}{q_t} = \frac{1}{k_2 q_e^2} + \frac{t}{q_e} \quad (2)$$

In the formula, q_e and q_t represent the adsorption capacities of the adsorbent for ARS and AF at equilibrium and at different times, respectively. The rate constants of K_1 (min^{-1}) and K_2 (g (mg min)$^{-1}$ for quasi-first-order and quasi-second-order models, respectively.

As shown in Fig. 8(a), the adsorption process could be divided into three stages, namely, rapid adsorption (0–2.5 min), slow adsorption (2.5–10 min), and equilibrium (after 10 min). Initially, ARS was rapidly captured due to the abundant active sites on the La_{12}-g-C_3N_4@β-SiC surface. During the slow adsorption stage, occupied sites increased the surface concentration of ARS, reducing the concentration gradient between the adsorbent and the solution, which weakened the mass transfer driving force and decreased the adsorption rate. Equilibrium

Table 1 Comparison chart of pollutants adsorbed by different catalysts

Entry	Catalysts	Pollutant	Stability	Time	Yield
1	(CoCuLDH)	RAN	8 times	60 min	70% (ref. 54)
2	D-SCR-G	MO	4 times	60 min	89.6% (ref. 55)
3	Mn–Ce–Co-Ox/PPS	PCDD/Fs	—	>6 h	78.01% (ref. 56)
4	g-C_3N_4/5-rGO/SnO_2	RhB	—	120 min	83.2% (ref. 57)
5	$Zn_2Ti_3O_8$/g-C_3N_4	RhB	—	90 min	89.0% (ref. 57)
6	Bi_2MoO_6	RhB	—	60 min	80% (ref. 58)
7	Ag-TiO_2	TOL	—	100 min	80% (ref. 59)
8	Graphene oxide-TiO_2 (GOT)	DDVP	—	80 min	80% (ref. 60)
9	TiO_2-TMAOH	MB	6 times	20 min	80% (ref. 61)
This work	La_{12}-g-C_3N_4@β-SiC	ARS	8 times	30 min	93.23%

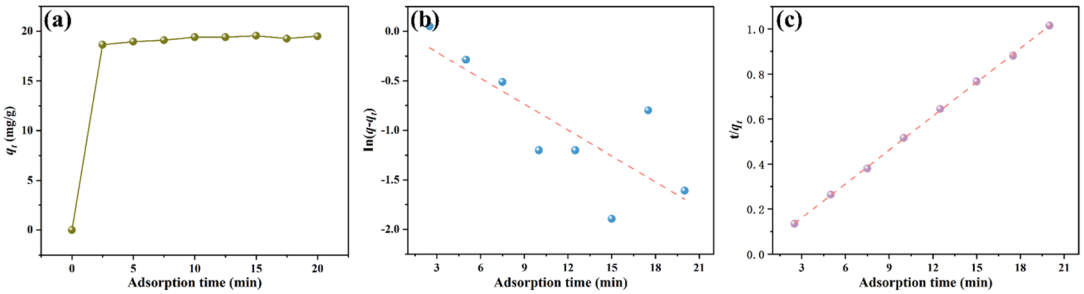

Fig. 8 (a) Adsorption kinetics curve (b) quasi-first-order kinetics (c) quasi-second-order kinetics model fitting curve of La_{12}-g-C_3N_4@β-SiC adsorbing ARS wastewater.

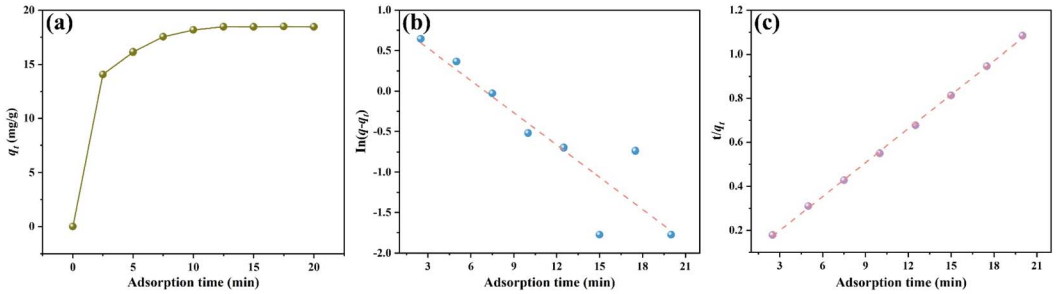

Fig. 9 (a) Adsorption kinetics curve (b) quasi-first-order kinetics (c) quasi-second-order kinetics model fitting curve of La_{12}-g-C_3N_4@β-SiC adsorbing AF wastewater.

Table 2 ARS adsorption kinetics parameters

Conc./(mg g^{-1})	Pseudo-first-order			Pseudo-second-order		
ARS	q_e (mg g^{-1})	K_1 (min $^{-1}$)	R^2	q_e (mg g^{-1})	K_1 (g (mg min)$^{-1}$)	R^2
20	1.1259	0.2012	0.5847	96.1538	0.0022	0.9997

was essentially reached after 10 minutes. The adsorption kinetics were further analyzed by fitting the data with pseudo-first-order and pseudo-second-order models, as presented in Fig. 8(b), (c), and Table 2. The results indicated that the pseudo-second-order model provided a better fit, with a higher correlation coefficient (R^2 = 0.9997). This indicated a positive correlation between the adsorption rate and the square of the number of adsorption sites. Combined with the thermodynamic analysis data, it could be inferred that this adsorption process was a single-layer adsorption and was mainly chemical adsorption.[62–64]

The adsorption kinetics of AF by La_{12}-g-C_3N_4@β-SiC are shown in Fig. 9(a), with the entire process reaching completion within 7.5 minutes. The adsorption data were fitted using pseudo-first-order and pseudo-second-order kinetic models, as presented in Fig. 9(b) and (c). Combined with the kinetic parameters in Table 3, the pseudo-second-order model demonstrates a better fit, effectively describing the adsorption kinetics of AF by La_{12}-g-C_3N_4@β-SiC, with a high correlation coefficient (R^2 = 0.9993).

3.4 Adsorption thermodynamic fitting and analysis

To evaluate the adsorption capacity for ARS and AF and characterize their adsorption behaviors, the Langmuir and Freundlich isotherm models were employed as standard analytical methods.

The Langmuir isotherm model is expressed as:

$$\frac{C_e}{q_e} = \frac{1}{q_m K_L} + \frac{C_e}{q_m} \quad (3)$$

In the Langmuir model equations, q_e (mg g^{-1}) denoted the equilibrium adsorption amount of the adsorbate (ARS or AF); q_m (mg g^{-1}) was the theoretical maximum adsorption capacity. C_e (mg g^{-1}) was the equilibrium solute concentration, and K_L (L mg^{-1}) was the Langmuir constant related to binding affinity. Furthermore, the essential feature of the Langmuir isotherm could be expressed by the dimensionless separation factor R_L, which described the type of isotherms,

$$R_L = \frac{1}{1 + K_L C_0} \quad (4)$$

In the formula, C_0 represented the initial concentration of the dye, and K_L (L mg^{-1}) was the Langmuir constant. The value of R_L

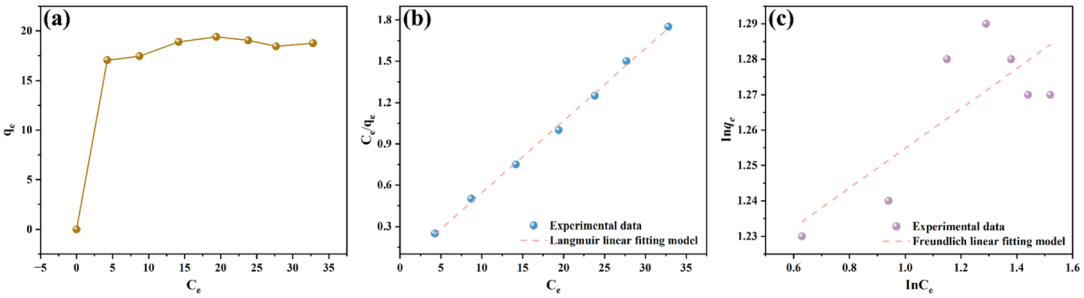

Fig. 10 The La_{12}-g-C_3N_4@β-SiC fitting curve of ARS (a) thermodynamic adsorption curve (b) Langmuir adsorption isotherm (c) Freundlich adsorption isotherm model.

Table 3 AF adsorption kinetics parameters

Conc./(mg g^{-1})	Pseudo-first-order			Pseudo-second-order		
AF	q_e (mg g^{-1})	K_1 (min^{-1})	R^2	q_e (mg g^{-1})	K_1 (g (mg $min)^{-1}$)	R^2
20	8.4807	0.3058	0.7973	22.6142	0.0380	0.9993

determined the feasibility of the adsorption process. The R_L value could indicate whether the process is irreversible ($R_L = 0$), beneficial ($0 < R_L < 1$), linear ($R_L = 1$), or unfavorable ($R_L > 1$).

The Freundlich adsorption model describes adsorption on heterogeneous surfaces, where the adsorbed molecules may interact.

The Freundlich isotherm model is expressed as:

$$\log q_e = \log K_F + \frac{1}{n}\log C_e \quad (5)$$

In the formula, K_F(L mg^{-1}) and n are the Freundlich constants related to adsorption capacity and adsorption intensity, respectively.

Fig. 10 shows the fitting curves of La_{12}-g-C_3N_4@β-SiC adsorption in ARS wastewater: they are respectively the thermodynamic adsorption curve, the Langmuir adsorption isotherm and the Freundlich adsorption isotherm model. Under the condition of 25 °C, the initial concentration of ARS was 5 mg L^{-1} to 35 mg L^{-1}, and the adsorption results of ARS were simulated by two models. The Langmuir equation and the Freundlich equation were tested, and the most suitable isotherm model was found. The results are shown in Fig. 10, and the Langmuir equation has a relatively high degree of fitting. In addition, Table 4 lists the parameters of the two models. It can also be seen from the correlation coefficient (R^2) that the Langmuir isotherm has a good fitting effect, indicating that the adsorption process of La_{12}-g-C_3N_4@β-SiC material on ARS is monolayer adsorption.

Fig. 11 showed the fitting curves of La_{12}-g-C_3N_4@β-SiC adsorption in AF wastewater: they were respectively the thermodynamic adsorption curve, the Langmuir adsorption isotherm and the Freundlich adsorption isotherm model. Under the condition of 25 °C, the initial concentration of AF was 5 mg L^{-1} to 35 mg L^{-1}, and the adsorption results of AF were simulated by two models. The Langmuir and Freundlich models were used for verification, and the results were shown in Fig. 11. The Langmuir equation had a relatively high degree of fitting. Table 5 listed the relevant parameters. It could be seen from the correlation coefficient (R^2) that the Langmuir isotherm had a good fit for AF adsorption, indicating that the AF adsorption process of La_{12}-g-C_3N_4@β-SiC material was monolayer adsorption (Table 5).

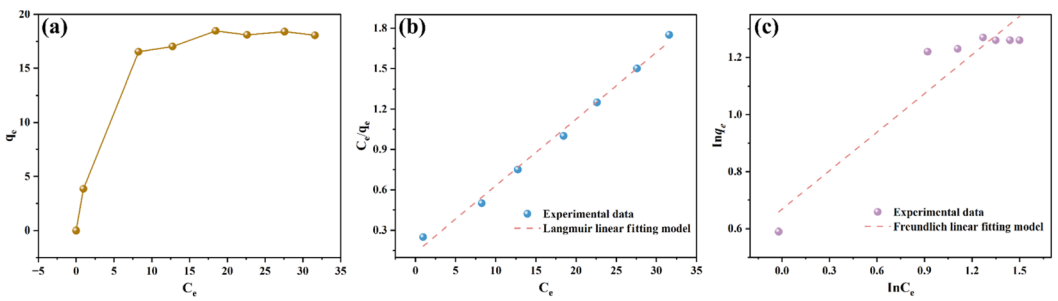

Fig. 11 The La_{12}-g-C_3N_4@β-SiC fitting curve of AF (a) thermodynamic adsorption curve (b) Langmuir adsorption isotherm (c) Freundlich adsorption isotherm model.

Table 4 ARS adsorption isotherm parameters

Conc./(mg L^{-1})	Langmuir-isotherm				Freundlich-isotherm		
ARS	q_{max} (mg g^{-1})	K_L (L mg^{-1})	R_L	R^2	n	K_F (Lmin $^{-1}$)	R^2
20	19.0730	2.6533	0.0185	0.9977	17.7715	3.3155	0.5609

Table 5 ARS adsorption isotherm parameters

Conc./(mg L^{-1})	Langmuir-isotherm				Freundlich-isotherm		
AF	q_{max} (mg g^{-1})	K_L (L mg^{-1})	R_L	R^2	n	K_F (L min^{-1})	R^2
20	20.1898	0.3663	0.1201	0.9919	2.2154	1.9495	0.8757

3.5 Adsorption pathways and mechanisms

To further understand the migration and transformation process of acid fuchsin dye in aquatic environments, it is crucial to clarify its adsorption pathways. Based on the data from the intermediate compounds detected by liquid chromatography-mass spectrometry (LC-MS), two possible adsorption pathways were proposed, as shown in Fig. 12. AF formed product A1 (m/z = 406) *via* decolorization. The π–π stacking effect between A1 and the aromatic ring led to decolorization or deamidation, resulting in product A2 (m/z = 381). A2 further reduced substituents on the aromatic ring to form product A3 (m/z = 274). A3 subsequently underwent ring opening to form product A4 (m/z = 267). As adsorption proceeded, the products eventually mineralized into CO_2 and H_2O. AF formed product B1 (m/z = 416) through modification of substituents. B1 continued to undergo charge transfer interaction with the AF molecule, resulting in ionization. This could be demonstrated by the continuous change in mass-to-charge ratio, namely products B2 (m/z = 340) and B3 (m/z = 338), but no covalent bonds were broken. Ultimately, these adsorption products mineralized into CO_2 and H_2O.

The possible adsorption mechanism of La_x-g-C_3N_4@β-SiC as the adsorbent for adsorbing AF was shown in Fig. 13. According to the characterization results of SEM and the analysis results of

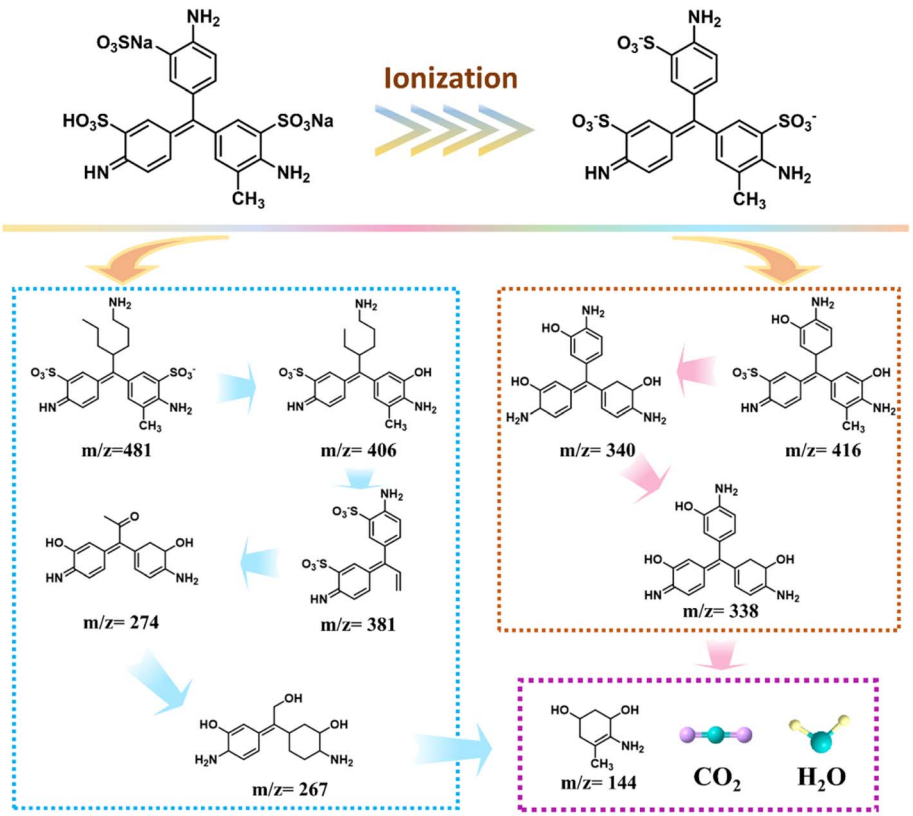

Fig. 12 Possible AF adsorption path diagram.

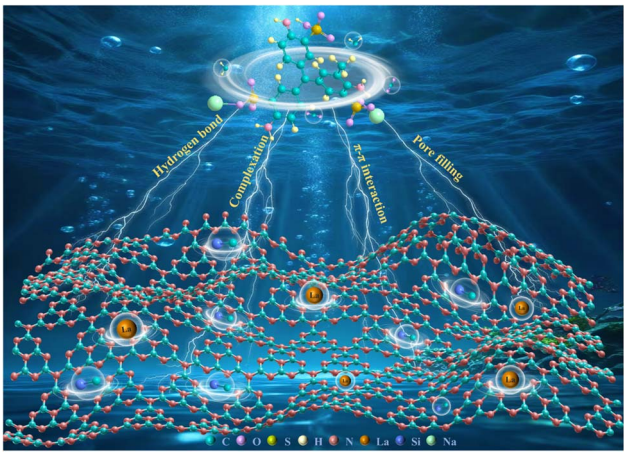

Fig. 13 Possible mechanism of AF adsorption by the La_x-g-C_3N_4@β-SiC adsorbent.

BET, there existed a rich and uniform mesoporous pore size structure in La_x-g-C_3N_4@β-SiC. Therefore, the influence of pore filling might be one of the reasons why the La_x-g-C_3N_4@β-SiC adsorption material could effectively adsorb AF. In addition, according to previous research reports, AF molecules could be tightly bound to the metal active sites on the adsorbent through electrostatic attraction.[58] Therefore, acidic fuchsin molecules might enhance the adsorption effect by forming coordination bonds with the metal La present in La_x-g-C_3N_4@β-SiC. Previous research results had shown that the hydroxyl groups in the intermediate after adsorption by AF molecules could interact with the nitrogen-containing components of the composite catalyst to form hydrogen bonds.[44] Furthermore, in the presence of aromatic rings on the adsorbent (La_x-g-C_3N_4@β-SiC) and the adsorbed dye (AF), π–π formed interactions between them (Fig. 13).

4. Conclusion

In this work, the La_{12}-g-C_3N_4@β-SiC composite adsorbent was prepared by thermal polymerization and mechanical methods. The characterization results of XRD, SEM, and XPS indicated that this material has a uniform-pore, layered structure. The composite material exhibited rapid and efficient adsorption capabilities for ARS and AF pollutants. Within 2.5 minutes, the removal rate of ARS reached 93.23%, and the removal rate of AF was 70.33%. The kinetic and thermodynamic analyses conformed to the pseudo-second-order model and Langmuir isotherm equation, consistent with the single-layer chemical adsorption mechanism. After 8 consecutive cycles, the average adsorption efficiency remained at 90%, demonstrating good stability and application potential. This research provides valuable insights into the design and application of composite materials for the removal of environmental pollutants.

Author contributions

Fanxia Zhang and Yuan Min conceived and designed the experiments; Fanxia Zhang operated the experiments; Zhiqiang Wu, Zhiliang Jin, and Jia Yang provided all the reagents and analysis tools; Yuan Min and Zhiqiang Wu completed the writing of this paper.

Conflicts of interest

The authors declare that they have no competing interests.

Data availability

The data supporting the findings of this study have been included within the article.

Acknowledgements

This work was financially supported by the Natural Science Foundation of the Ningxia Hui Autonomous Region (2024AAC03314, 2026AAC030892); the Firstclass Discipline Construction (Education Discipline) in Higher Education Institutions of Ningxia (NXYLXK2021B10), the Major Project of "Leading the Charge with Open Competition" for Undergraduate Education Reform at Ningxia Normal University (BKJXGG202503) and College student innovation and entrepreneurship training program project (G202510753016; S202510753012).

References

1 A. P. Periyasamy, Recent advances in the remediation of textile-dye-containing wastewater: prioritizing human health and sustainable wastewater treatment, *Sustainability*, 2024, **16**(2), 495, DOI: 10.3390/su16020495.
2 F. Uddin, Environmental hazard in textile dyeing wastewater from local textile industry, *Cellulose*, 2021, **28**, 10715–10739, DOI: 10.1007/s10570-021-04228-4.
3 T. Islam, M. R. Repon, T. Islam, Z. Sarwar and M. M. Rahman, Impact of textile dyes on health and ecosystem: a review of structure, causes, and potential solutions, *Environ. Sci. Pollut. Res.*, 2023, **30**(4), 9207–9242, DOI: 10.1007/s11356-022-24398-3.
4 J. Zhang, Y. Chi and L. Feng, The mechanism of degradation of alizarin red by a white-rot fungus *Trametes gibbosa*, *BMC Biotechnol.*, 2021, **21**, 64, DOI: 10.1186/s12896-021-00720-8.
5 S. Akbarnejad, A. A. Amooey and S. Ghasem, High effective adsorption of acid fuchsin dye using magnetic biodegradable polymer-based nanocomposite from aqueous solutions, *Microchem. J.*, 2019, **149**, 103966, DOI: 10.1016/j.microc.2019.103966.
6 F. Kordbacheh and G. Heidari, Water pollutants and approaches for their removal, *Mater. Chem. Horiz.*, 2023, **2**(2), 139–153, DOI: 10.22128/mch.2023.684.1039.
7 M. F. Hanafi and N. Sapawe, A review on the current techniques and technologies of organic pollutants removal from water/wastewater, *Mater. Today Proc.*, 2020, **31**, 158–165, DOI: 10.1016/j.matpr.2021.01.265.
8 S. R. Carpenter, E. H. Stanley and M. J. Vander Zanden, State of the world's freshwater ecosystems: physical, chemical,

and biological changes, *Annu. Rev. Environ. Resour.*, 2011, **36**(1), 75–99, DOI: 10.1146/annurev-environ-021810-094524.

9 T. Kopac, Emerging applications of process intensification for enhanced separation and energy efficiency, environmentally friendly sustainable adsorptive separations: a review, *Int. J. Energy Res.*, 2021, **45**(11), 15839–15856, DOI: 10.1002/er.6944.

10 R. Rashid, I. Shafiq, P. Akhter, M. J. Iqbal and M. Hussain, A state-of-the-art review on wastewater treatment techniques: the effectiveness of adsorption method, *Environ. Sci. Pollut. Res.*, 2021, **28**(8), 9050–9066, DOI: 10.1007/s11356-021-12395-x.

11 S. Satyam and S. Patra, Innovations and challenges in adsorption-based wastewater remediation: a comprehensive review, *Heliyon*, 2024, **10**(9), e29573, DOI: 10.1016/j.heliyon.2024.e29573.

12 C. Shen, C. Chen, T. Wen, Z. Zhao, X. Wang and A. Xu, Superior adsorption capacity of g-C_3N_4 for heavy metal ions from aqueous solutions, *J. Colloid Interface Sci.*, 2015, **456**, 7–14, DOI: 10.1016/j.jcis.2015.06.004.

13 H. Xie, J. Zhang, D. Wang, J. Liu, L. Wang and H. Xiao, Construction of three-dimensional g-C_3N_4 attapulgite hybrids for Cd(II) adsorption and the reutilization of waste adsorbent, *Appl. Surf. Sci.*, 2020, **504**, 144456, DOI: 10.1016/j.apsusc.2019.144456.

14 E. Fernandes, J. Gomes and R. C. Martins, Semiconductors application forms and doping benefits to wastewater treatment: a comparison of TiO_2, WO_3, and g-C_3N_4, *Catalysts*, 2022, **12**, 1218, DOI: 10.3390/catal12101218.

15 S. Guo, N. Duan, Z. Dan, G. Chen, F. Shi and W. Gao, g-C_3N_4 modified magnetic Fe_3O_4 adsorbent: preparation, characterization, and performance of Zn(II), Pb(II) and Cd(II) removal from aqueous solution, *J. Mol. Liq.*, 2018, **258**, 225–234, DOI: 10.1016/j.molliq.2018.03.029.

16 A. Fdez-Sanromán, M. Pazos, E. Rosales and A. Sanromán, Pushing the operational barriers for g-C_3N_4: a comprehensive review of cutting-edge immobilization strategies, *Catalysts*, 2024, **14**, 175, DOI: 10.3390/catal14030175.

17 X. Qian, W. Li, X. Wang, H. Guan, Q. Bao, B. Zhao, B. Wulan, S. Liu, D. Zhu, X. Feng and J. Sun, Multifunctional roles of ionic microenvironments in the preparation, modification, and application of g-C_3N_4, *Adv. Funct. Mater.*, 2025, **35**(11), 2416946, DOI: 10.1002/adfm.202416946.

18 G. Dong, Y. Zhang, Q. Pan and J. Qiu, A fantastic graphitic carbon nitride (g-C_3N_4) material: electronic structure, photocatalytic and photoelectronic properties, *J. Photochem. Photobiol., A*, 2014, **20**, 33–50, DOI: 10.1016/j.jphotochemrev.2014.04.002.

19 S. Cao and J. Yu, g-C_3N_4-based photocatalysts for hydrogen generation, *J. Phys. Chem. Lett.*, 2014, **5**(12), 2101–2107, DOI: 10.1021/jz500546b.

20 J. Dong, Y. Zhang, M. I. Hussain, W. Zhou, Y. Chen and L.-N. Wang, g-C_3N_4: properties, pore modifications, and photocatalytic applications, *Nanomaterials*, 2021, **12**(1), 121, DOI: 10.3390/nano12010121.

21 A. Hayat, M. Sohail, A. El Jery, K. M. Al-Zaydi, K. F. Alshammari, J. Khan, H. Ali, Z. Ajmal, T. A. Taha, I. U. Din, R. Altamimi, M. A. Hussein, Y. Al-Hadeethi, Y. Orooji and M. Z. Ansari, Different dimensionalities, morphological advancements and engineering of g-C_3N_4-based nanomaterials for energy conversion and storage, *Chem. Rec.*, 2023, **23**(5), e202200171, DOI: 10.1002/tcr.202200171.

22 N. Wang, L. Cheng, Y. Liao and Q. Xiang, Effect of functional group modifications on the photocatalytic performance of g-C_3N_4, *Small*, 2023, **19**(27), 2300109, DOI: 10.1002/smll.202300109.

23 G. Tuci, Y. Liu, A. Rossin, X. Guo, C. Pham, G. Giambastiani and C. Pham-Huu, Porous silicon carbide (SiC): a chance for improving catalysts or just another active-phase carrier, *Chem. Rev.*, 2021, **121**(17), 10559–10665, DOI: 10.1021/acs.chemrev.1c00269.

24 P. Nguyen and C. Pham, Innovative porous SiC-based materials: from nanoscopic understandings to tunable carriers serving catalytic needs, *Appl. Catal., A*, 2011, **391**(1–2), 443–454, DOI: 10.1016/j.apcata.2010.07.054.

25 H. Liang, J. Wang, W. Wang, Y. Wang, X. Deng, Z. Xue, Y. Sun, G. He and X. Ruan, N-doping enriched porous MgO-modified biochar enables efficient anionic acid fuchsin dye removal, *Sep. Purif. Technol.*, 2024, **335**, 126180, DOI: 10.1016/j.seppur.2023.126180.

26 Z. Wu, Y. Li, X. Li, E. Feng, L. Cao, Z. Li, X. Wang, P. Jiang and D. Wang, Acid protonation promoted different crystal phase structure silicon carbide-based carbon nitride composites to enhance the photocatalytic degradation of dye wastewater, *RSC Adv.*, 2023, **13**(51), 35990–36001, DOI: 10.1039/d3ra06438g.

27 N. D. Shcherban, Review on synthesis, structure, physical and chemical properties and functional characteristics of porous silicon carbide, *J. Ind. Eng. Chem.*, 2017, **50**, 15–28, DOI: 10.1016/j.jiec.2017.02.002.

28 Z. Wu, W. Liu, G. Wang, *et al.*, Preparation of protonated g-C_3N_4/β-SiC composite and its photocatalytic performance for degradation of alizarin red, *Chem. Res. Chin. Univ.*, 2019, **40**(10), 2178–2185, DOI: 10.1016/j.cclet.2024.109924.

29 B. Song, J. Wang, J. Qiu, Y. Nie, P. Li, Y. Zhu, C. Yan, Z. Xie, G. Chen and Z. Le, *Appl. Surf. Sci.*, 2025, **684**, 161763, DOI: 10.1016/j.apsusc.2024.161763.

30 F. Chang, J. Zheng, X. Wang, Q. Xu, B. Deng, X. Hu and X. Liu, Heterojuncted non-metal binary composites silicon carbide/g-C_3N_4 with enhanced photocatalytic performance, *Mater. Sci. Semicond. Process.*, 2018, **75**, 183–192, DOI: 10.1016/j.mssp.2017.11.043.

31 H. Xua, Z. Gan, W. Zhou, Z. Ding and X. Zhang, A metal-free 3C-SiC/g-C_3N_4 composite with enhanced visible light photocatalytic activity, *RSC Adv.*, 2017, **7**(63), 40028–40033, DOI: 10.1039/C7RA06497G.

32 B. Wang, J. Zhang and F. Huang, Enhanced visible light photocatalytic H_2 evolution of metal-free g-C_3N_4/SiC heterostructured photocatalysts, *Appl. Surf. Sci.*, 2017, **391**, 449–456, DOI: 10.1016/j.apsusc.2016.07.056.

33 H. Guo, S. Gao, X. Chai, Y. Shi and J. Gao, Preparation of Z-type heterojunction SiC f/g-C_3N_4 composites with enhanced photocatalytic degradation of tetracycline under visible light, *Appl. Organomet. Chem.*, 2023, **37**(3), e7022, DOI: 10.1002/aoc.7022.

34 M. Xue, J. Han, X. Dai, Y. Ge, Y. Zhang and Z. Hai, Construction of Cu_2O ternary composite comprising SiC and g-C_3N_4 for improved photocatalytic degradation of methyl orange *via* synergetic Z-scheme effect, *Opt. Mater.*, 2024, **155**, 115883, DOI: 10.1016/j.optmat.2024.115883.

35 H. Zhu, B. Yang, J. Yang, Y. Yuan and J. Zhang, Persulfate-enhanced degradation of ciprofloxacin with SiC/g-C_3N_4 photocatalyst under visible light irradiation, *Chemosphere*, 2021, **276**, 130217, DOI: 10.1016/j.chemosphere.2021.130217.

36 H. Shao, M. Heng, J. Guo, R. Yang, H. Zhang, J. Fan, G. Li, Y. Miao and S. Xiao, 3D interwoven SiC/g-C_3N_4 structure for superior charge separation and CO_2 photoreduction performance, *Langmuir*, 2024, **41**(1), 1115–1125, DOI: 10.1021/acs.langmuir.4c04436.

37 J. Pan, Y. Zhang, Y. Guan, Y. Yan, H. Tang, X. Liu, M. Wang and X. Wei, Multifunctional Ni nanoparticles decorated SiC nanofibers/g-C_3N_4 nanosheets heterojunctions for drastically increased LED-light-driven hydrogen generation, *Appl. Surf. Sci.*, 2022, **579**, 152171, DOI: 10.1016/j.apsusc.2021.152171.

38 S. Jayakumari and M. Tangstad, Transformation of β-SiC from charcoal, coal, and petroleum coke to α-SiC at higher temperatures, *Metall. Mater. Trans. B*, 2020, **51**, 2673–2688, DOI: 10.1007/s11663-020-01970-1.

39 C. Yan, H. Zhao, D. F. Perepichka and F. Rosei, Lanthanide ion doped upconverting nanoparticles: synthesis, structure and properties, *Small*, 2016, **12**(29), 3888–3907, DOI: 10.1002/smll.201601565.

40 X. Yin, X. Li, E. Petropoulos, Y. Feng, B. Yang, L. Xue, L. Yang and S. He, Phosphate removal from actual wastewater *via* La(OH)$_3$-C_3N_4 adsorption: performance, mechanisms and applicability, *Sci. Total Environ.*, 2022, **814**(25), 152791, DOI: 10.1016/j.scitotenv.2021.152791.

41 S. B. Prasanna, R. Sakthivel, S. A. Shivamurthy, Y.-C. Lin, X. Liu, J.-C. Chen, T.-Y. Liu and R.-J. Chung, Catalytic degradation of tetracycline using marigold flower-like structure erbium molybdate decorated on sulphur-doped g-C_3N_4 nanocomposite: kinetics, thermodynamics, DFT calculations, and toxicity studies, *Sep. Purif. Technol.*, 2024, **330**, 125439, DOI: 10.1016/j.seppur.2023.125439.

42 X. Yu, Z. Song, X. Dong, H. Li, H. Liu, B. Zhao, T. Ye, Y. Jiang, X. Li, L. Duan, J. Fan and P. Zhao, Enhanced photocatalytic activity of rare earth (Yb, Nd and Ce)-doped g-C_3N_4 nanosheets for the degradation of organic dyes under visible light, *J. Mater. Sci.: Mater. Electron.*, 2022, **33**, 13271–13289, DOI: 10.1007/s10854-022-08267-w.

43 Z. Wu, W. Liu, G. Wang, W. Cai, X. Yue, H. Zhan, S. Bi, Z. Meng and B. Ma, Preparation of protonated g-C_3N_4/β-SiC composites and photocatalytic degradation of alizarin red S, *Chem. J. Chin. Univ.*, 2019, **40**(10), 2178–2185, DOI: 10.7503/cjcu20190215.

44 Z. Wu, Y. Li, P. Jiang, S. Ma, W. Dong, H. Zhao, E. Feng and X.-M. Wang, Evaluation of the adsorption and degradation performance of lanthanum-modified mesoporous carbon nitride composite materials for tetracycline wastewater treatment, *New J. Chem.*, 2024, **48**, 9090–9102, DOI: 10.1039/D4NJ00864B.

45 Z. Wu, Y. Li, X. Li, E. Feng, L. Cao, Z. Li, X. Wang, P. Jiang and D. Wang, Acid protonation promoted different crystal phase structure silicon carbide-based carbon nitride composites to enhance the photocatalytic degradation of dye wastewater, *RSC Adv.*, 2023, **13**, 35672–35682, DOI: 10.1039/D3RA06438G.

46 M. A. Fathy, S. M. Abdelbasir, S. S. Hassan and A. H. Kamel, Mechanochemical activation for lead extraction from spent cathode ray tube, *J. Mater. Cycles Waste Manage.*, 2021, **23**, 1090–1101, DOI: 10.1007/s10163-021-01198-4.

47 Y. Li, F. Liu, M. Li, W. Li, X. Qi, M. Xue, Y. Wang and F. Han, Study on adsorption coupling photodegradation on hierarchical nanostructured g-C_3N_4, TiO_2, activated carbon fiber composites for toluene removal, *J. Sol-Gel Sci. Technol.*, 2020, **93**(2), 402–418, DOI: 10.1007/s10971-019-05198-7.

48 J.-Y. Kang, W. Ha, H.-X. Zhang and Y.-P. Shi, Sandwich-like, potassium(I) doped g-C_3N_4 with tunable interlayer distance as a high selective extractant for the determination of Ba(II), *Talanta*, 2020, **215**, 120916, DOI: 10.1016/j.talanta.2020.120916.

49 T. Feng, C. Li, X. Li, B. Wang and E. Liu, Preparation and performance of SiC coating on C/C composite, *Mater. Sci. Eng., B*, 2025, **319**, 118354, DOI: 10.1016/j.mseb.2025.118354.

50 M. Zhang, Quasi-monodisperse β-SiC nanospheres: synthesis and application in chemical-mechanical polishing, *J. Phys. Chem. Solids*, 2017, **103**, 1–5, DOI: 10.1016/j.jpcs.2016.11.026.

51 X. Fu and D. Wang, Effect of stacking fault nanolayers on the photoluminescence properties of SiC nanowires, *Appl. Surf. Sci.*, 2019, **493**, 497–505, DOI: 10.1016/j.apsusc.2019.07.019.

52 Z. Yang, L. Li, H. Yu, M. Liu, Y. Chi, J. Sha and S. Xu, Facile synthesis of highly crystalline g-C_3N_4 nanosheets with remarkable visible light photocatalytic activity for antibiotics removal, *Chemosphere*, 2021, **271**, 129503, DOI: 10.1016/j.chemosphere.2020.129503.

53 H. Xie, J. Zhang, D. Wang, J. Liu, L. Wang and H. Xiao, Construction of three-dimensional g-C_3N_4 attapulgite hybrids for Cd(II) adsorption and the reutilization of waste adsorbent, *Appl. Surf. Sci.*, 2020, **504**, 144456, DOI: 10.1016/j.apsusc.2019.144456.

54 A. Sharmin, M. B. Asif, G. Zhang, M. A. Bhuiyan and B. Pramanik, *Environ. Sci. Pollut. Res.*, 2024, **49**, 28343–28360, DOI: 10.1007/s11356-024-34331-5.

55 Y. Li, C. Wang, Z. Zhang, H. Liu, J. Chen, L. Sun and Q. Zhang, *Chem. Phys. Lett.*, 2024, **840**, 141158, DOI: 10.1016/j.cplett.2024.141158.

56 H. Liu, Y. Peng, J. Tao, J. Yang, X. Zhang, L. Wang and C. Li, *Chin. J. Chem. Eng.*, 2021, **72**, 1018–1025, DOI: 10.11949/0438-1157.20201294.

57 P. Kumari, *et al.*, Recent overview of solar photocatalysis and solar photo-Fenton processes for wastewater treatment, *Molecules*, 2024, **29**(16), 3836, DOI: 10.3390/molecules29163836.

58 V. Sasikala, S. Sarala, P. Karthik, N. Prakash and A. Mukkannan, Photocatalytic degradation of Rhodamine-B and crystal violet in wastewater: a sustainable approach using bismuth molybdate, *Emergent Mater.*, 2024, **7**(6), 2523–2534, DOI: 10.1007/s42247-024-00749-3.

59 H. Tian, X. Xi, P. Dong, X. Cai and Y. Liu, A comparison of photocatalytic degradation of different environmental pollutants by Ag-TiO_2 photocatalyst, *J. Nanosci. Nanotechnol.*, 2017, **17**(7), 4716–4723, DOI: 10.1166/jnn.2017.13785.

60 R. Kumar, L. George, Z. Jun and S. Mukherji, Photocatalytic activity of graphene oxide-TiO_2 nanocomposite on dichlorvos and malathion and assessment of toxicity changes due to photodegradation, *Chemosphere*, 2022, **308**, 136575, DOI: 10.1016/j.chemosphere.2022.136575.

61 K. Sonu, S. H. Puttaiah, V. S. Raghavan and S. S. Gorthi, Photocatalytic degradation of MB by TiO_2: studies on recycle and reuse of photocatalyst and treated water for seed germination, *Environ. Sci. Pollut. Res.*, 2021, **28**, 48742, DOI: 10.1007/s11356-021-13863-0.

62 H. Zhang, Q. Mu, X. Yu, K. Zhou, X. Chen, H. Hao and Y. Li, Effect of particle size and composition on the dielectric properties of SiC/PVDF composites, *Polymers*, 2022, **14**, 5458, DOI: 10.3390/polym14245458.

63 G. Tian, W. Wang, L. Zong and A. Wang, Macroporous TiO_2/carbon composites prepared *via* a simple soaking-carbonization method for the adsorption of uranium (VI), *J. Environ. Chem. Eng.*, 2017, **5**, 1024–1031, DOI: 10.1016/j.jece.2017.01.028.

64 K. Fan, T. Zhang, S. Xiao, H. He, J. Yang and Z. Qin, Preparation and properties of carboxymethyl chitosan/alginate composite hydrogels for wound healing, *Int. J. Biol. Macromol.*, 2022, **210**, 381–391, DOI: 10.1016/j.ijbiomac.2022.05.042.